Faraday Discussions

Cite this: *Faraday Discuss.*, 2023, **242**, 231

PAPER

Joint electric and magnetic beam deflection experiments and quantum chemical studies of MSn_{12} clusters (M = Al, Ga, In): on the interplay of geometric structure and magnetic properties in nanoalloys†

Filip Rivic, ‡* Andreas Lehr, ‡ Thomas M. Fuchs and Rolf Schäfer

Received 3rd May 2022, Accepted 10th June 2022
DOI: 10.1039/d2fd00091a

MSn_{12} clusters (M = Al, Ga, In) were studied in electric and magnetic beam deflection experiments at temperatures of 16 K and 30 K. For all three species, the results of the electric beam deflection experiments indicate the presence of two structural isomers of which one is considerably polar. The magnetic beam deflection experiments show atom-like beam splitting (superatomic behavior) with *g*-factors of 2.6–2.7 for a fraction of the clusters in the molecular beam, indicating significant spin–orbit coupling. On the one hand, we investigate by several experiments combining electric and magnetic deflectors how the superatomic and polar fractions are linked proving the correlation of the Stark and Zeeman effects. On the other hand, the magnetic deflection behavior is examined more thoroughly by performing quantum chemical calculations. By systematic distortion of an artificial icosahedral tin cage towards the global minimum structure, which has a pyritohedral geometry, the shifts in the magnitude of the *g*-factor are found to be mainly caused by a single dominant electronic excitation. This allows one to develop a semi-quantitative understanding of the magnetic behavior. On the basis of avoided crossings in the rotational Zeeman diagram, simulations of the magnetic beam deflection comprising computed rotational constants, vibrational modes, *g*-factors and spin–rotation coupling constants are performed which resemble our experimental findings in satisfactory agreement. With this, a better understanding of the magnetic properties of nanoalloy clusters can be achieved. However, the geometric structures of the polar isomers are still unknown.

Technical University of Darmstadt, Eduard-Zintl-Institut, Alarich-Weiss-Straße 8, 64287 Darmstadt, Germany. E-mail: filip.rivic@tu-darmstadt.de; andreas.lehr@tu-darmstadt.de

† Electronic supplementary information (ESI) available: In-depth computational details, cartesian coordinates and extended list of $AlSn_{12}$ structural isomers as well as further information on MO diagrams and *g*-factors. See DOI: https://doi.org/10.1039/d2fd00091a

‡ These authors contributed equally to this work.

1 Introduction

Electric and magnetic beam deflection experiments are well established tools to investigate the Stark and Zeeman effects of isolated atoms and clusters.[1–6] In this way, the dielectric and magnetic susceptibilities can be determined, in order to systematically study the influence of size,[7,8] geometry[9–11] and chemical composition[12–14] on the dielectric and magnetic behavior of nanoalloy clusters.

In order to work out the interplay between geometric structure and magnetic properties, single p-doped tetrel clusters are studied experimentally and quantum chemically. Such doped clusters are ideal model systems to better understand the interaction of an individual paramagnetic defect in a diamagnetic host on the nanoscale. Group 13 elements (Al, Ga, In) act as dopant atoms, which form endohedral complexes with tin clusters.[15–17] Taking the bimetallic species MSn_{12} with M = Al, Ga, In as examples, we systematically investigate which structural isomers are formed and how the geometric arrangement of the atoms affects the magnetic properties, the *g*-factor in particular. For this purpose, molecular beam experiments are used together with theoretical methods for global optimization as well as the description of the magnetic properties. On the one hand, the experimental work focuses on measuring the Stark effect in order to discriminate the geometric structure of the isomers present. On the other hand, the magnetic behavior is studied using Stern–Gerlach experiments. The combination of electric and magnetic deflection experiments proves the existence of a nonpolar and a polar structural isomer and allows the correlation between the Stark and Zeeman effects of these two isomers to be studied. In a previous work on $AlSn_{12}$, this approach revealed not only the presence of two structural isomers in the molecular beam experiments but also an interdependency of the nonpolar and superatomic properties.[16] With the help of a global optimization strategy, an attempt is then made to clarify the spatial arrangement of the atoms in the two isomers. Since the nonpolar isomers show superatomic behavior at low temperatures, they are ideally suited to reveal correlations between the geometric and the electronic structure and thus also the magnetic behavior. In particular, the spin density on the doping atoms and the *g*-factor of the bimetallic clusters depend sensitively on the spatial arrangement of the atoms. The observed correlation can be interpreted semi-quantitatively by considering spin–orbit effects. Hence, the impact of spin–orbit coupling on the analysis of the magnetic deflection behavior of isolated nanoalloy clusters is considered for the first time.

2 Experiment and theory

2.1 Experimental methods

The experimental setup is described in detail elsewhere,[5,17–19] therefore only a brief overview is given here. The molecular beam is generated in a pulsed laser vaporization source (LVS) by focusing a frequency-doubled Nd:YAG laser onto a rotating and translating alloyed target rod containing 5 at% aluminum, gallium or indium in tin. Helium gas is fed to the emerging plasma through a pulsed valve and clusters are formed in an aggregation chamber. The helium–cluster mixture is thermalized in a cryogenic nozzle with a temperature T_{nozzle} of 16 K or 30 K and expands through a double-skimmer into high vacuum. The molecular beam

passes two collimating slits before going through two deflection units with either an inhomogeneous electric field ($d\Gamma_{el}/dz = 4 \times 10^9$ V m^{-2}) or magnetic field ($d\Gamma_{mag}/dz = 349$ Tm^{-1}) applied. Both are generated by a two-wire geometry.[20,21] The clusters are ionized by an F_2 excimer laser and detected in a time-of-flight mass spectrometer (TOF-MS). The deflection is probed by a scanning slit unit just before photoionization. The positions of the scanning slit are approached in random order. First, a mass spectrum without field is recorded. Then, at the same position, the field is applied and the deflected beam profile is measured directly afterwards. In order to compare several beam profiles from independent experimental runs, the measured deflection $d_{i,z}$ of a cluster species is converted to the mean projection of the dipole moment $\bar{\mu}_{i,z}$ on the field direction

$$\bar{\mu}_{i,z} = \frac{d_{i,z} m v_x^2}{\frac{l_{i,1}^2}{2} + l_{i,1} l_{i,2}} \left(\frac{d\Gamma_i}{dz}\right)^{-1}, \quad (1)$$

with cluster mass m, field length $l_{i,1}$, drift length $l_{i,2}$, electric or magnetic field Γ_i and $i \in \{el, mag\}$. Note that $\bar{\mu}_{i,z}$ is proportional to $d_{i,z}$ but allows a depiction of several deflection profiles together independent of the velocities v_x. The latter is measured with a mechanical shutter based on a hard drive disk.[22]

2.2 Computational methods

The conducted calculations comprise the genetic algorithm for scanning the coordination space in order to obtain suitable structural candidates, a reoptimization and frequency analysis on a higher level of theory including the calculation of geometric and dielectric properties as well as the computation of magnetic properties. Only a compact presentation of the applied methodology will be given here and for extensive technical details readers are referred to the ESI.†

The global optimization was performed using the German Improved Genetic Algorithm (GIGA)[23] based on spin-restricted plane-wave density functional theory (DFT) using Quantum Espresso v6.4.1 [24,25] incorporating the PBE exchange–correlation (xc) functional.[26,27] All identified structural candidates were then locally reoptimized using spin-unrestricted Gaussian orbital DFT at the PBE0/def2-TZVPP[28–30] level of theory in Gaussian16 [31] as well as Orca v5.0.2.[32–34] The choice of the xc functional/basis set combination was justified by extensive previous studies on bare tin,[35–38] bare lead[10,39] and doped tin clusters.[14,40–42] Energetically-relevant isomers were considered for the calculation of electric dipole moments, unrestricted spin densities and vibrational frequencies. DLPNO-CCSD(T)/cc-pVTZ-PP[43–48] single-point energies were additionally computed as implemented in Orca. The computation of the *g*-matrix and the hyperfine coupling constant were done within the EPR/NMR module of Orca employing the scalar relativistically-parametrized second-order Douglas–Kroll–Hess (DKH2)[49] and zeroth-order regular approximation (ZORA) Hamiltonians.[50] It was assured that geometry optimizations for all structural isomers at the relativistic level yield insignificant differences to the nonrelativistic PBE0/def2-TZVPP results. Furthermore, the spin–orbit coupling operators are treated by the spin–orbit mean field (SOMF) approach.[51] The *g*-matrices were calculated both at the DKH-PBE0/(SARC-)DKH-def2-TZVPP and ZORA-PBE0/(SARC-)ZORA-def2-TZVPP level of theory,[52,53] yielding very similar results, whereas hyperfine coupling constants were only obtained using the ZORA method.

2.3 Theory of magnetic properties

Magnetic deflection experiments on superatomic clusters allow the cluster's electronic *g*-factor to be determined.[16,54–58] Additionally, they shine light on the hyperfine and (electron) spin–rotation coupling to some extent.[55,59–64] All three quantities are of key importance in describing and interpreting the experimental deflection data. In this study, an effort was made to provide a computational routine for accessing these properties with DFT calculations. Theoretically, these properties are introduced in the phenomenological spin Hamiltonian $\hat{H}_{\mathrm{Spin}}$ with μ_{B} being the Bohr magneton, $\boldsymbol{B}$ the magnetic flux density, $\boldsymbol{g}$ the *g*-matrix, $\hat{\boldsymbol{S}}$ the fictitious spin operator, $\boldsymbol{A}^{(\mathrm{A})}$ the hyperfine coupling matrix of nucleus A, $\hat{\boldsymbol{I}}^{(\mathrm{A})}$ the nuclear spin operator of nucleus A, $\boldsymbol{\Delta}^{\mathrm{SR}}$ the (electron) spin–rotation coupling matrix and $\hat{\boldsymbol{J}}$ the total rotational angular momentum operator.

$$\hat{H}_{\mathrm{Spin}} = \mu_{\mathrm{B}}\boldsymbol{B}\boldsymbol{g}\hat{\boldsymbol{S}} + \sum_{A}\hat{\boldsymbol{S}}\boldsymbol{A}^{(\mathrm{A})}\hat{\boldsymbol{I}}^{(A)} + \hat{\boldsymbol{S}}\boldsymbol{\Delta}^{\mathrm{SR}}\hat{\boldsymbol{J}} \tag{2}$$

The strategy is to first construct a "true" Hamiltonian containing the nonrelativistic Born–Oppenheimer (BO) contribution, the relativistic contribution, composed of the scalar-relativistic part incorporating the DKH2 or ZORA method as well as the effective spin–orbit part, and the magnetic field-dependent contribution. By comparison of this Hamiltonian with the spin Hamiltonian of eqn (2), sum-over-states (SOS) expressions for the three properties can be derived.[65–69] Following this procedure, only the *g*-matrix and the hyperfine coupling matrix $\boldsymbol{A}^{(\mathrm{A})}$ are computed specifically, whereas the spin–rotation coupling matrix $\boldsymbol{\Delta}^{\mathrm{SR}}$ is estimated from Curl's perturbative treatment[70,71] which links it to the *g*-matrix elements, once calculated, *via*

$$g_{ab} = g_{\mathrm{e}}\delta_{ab} - \frac{1}{\hbar^2}\sum_{k}\Delta^{\mathrm{SR}}_{ak}I_{kb}, \tag{3}$$

with g_{e} being the free-electron *g*-factor and I_{ab} the elements of the inertial tensor with $a, b \in \{x, y, z\}$. Since the hyperfine coupling constant is solely calculated to give a precise measure of the atom-specific ground-state spin density, owing to the Fermi-contact contribution becoming the dominant part, readers are referred to the literature for computational details.[69,72] Hence, the evaluation of the *g*-matrix is the main focus of this study.

Spin–orbit coupling (SOC) effects are crucial for the prediction of magnetic properties and their treatment requires particular care. In the case of the *g*-matrix the magnetic-field dependent contribution is given by the spin- and orbital-Zeeman Hamiltonian.[68,73] It is well known that the *g*-matrix can be subdivided into $\boldsymbol{g} = g_{\mathrm{e}}\mathbf{1} + \Delta\boldsymbol{g}^{(\mathrm{RMC})} + \Delta\boldsymbol{g}^{(\mathrm{GC})} + \Delta\boldsymbol{g}^{(\mathrm{OZ/SOC})}$ with $\Delta\boldsymbol{g}^{(\mathrm{RMC})}$ being the relativistic mass correction, $\Delta\boldsymbol{g}^{(\mathrm{GC})}$ the gauge correction and $\Delta\boldsymbol{g}^{(\mathrm{OZ/SOC})}$ the orbital-Zeeman–spin–orbit coupling cross term arising to second order[68] and making up >99% of the total Δg-shift for the studied clusters. It can be shown[67,69] that the SOS expression following the selection rule $\Delta S = S_0 - S_n = 0$, with S_0 referring to the spin quantum number of the electronic ground state (later on simply S) and S_n to the spin quantum number of the nth excited electronic state, is given by

$$\Delta g_{ab}^{(\mathrm{OZ/SOC})} = -\frac{1}{S_0}\sum_n \Delta_n^{-1}\delta_{S_0S_n} \times\left\{\left\langle\psi_0^{S_0S_0}\middle|\sum_i \hat{l}_{i,a}\middle|\psi_n^{S_nS_n}\right\rangle\left\langle\psi_n^{S_nS_n}\middle|\sum_{i,A}\xi(r_{iA})\hat{l}_{iA,b}\hat{s}_{i,0}\middle|\psi_0^{S_0S_0}\right\rangle + \left\langle\psi_0^{S_0S_0}\middle|\sum_{i,A}\xi(r_{iA})\hat{l}_{iA,a}\hat{s}_{i,0}\middle|\psi_n^{S_nS_n}\right\rangle\left\langle\psi_n^{S_nS_n}\middle|\sum_i \hat{l}_{i,b}\middle|\psi_0^{S_0S_0}\right\rangle\right\}. \quad (4)$$

Here, $\Delta_n = E_n - E_0$ is the energy difference between the ground and excited states. The electronic wavefunction $\psi_{\mathrm{I}}^{\mathrm{SM}}$ of state I is written for the standard state of the magnetic spin quantum number $M_S = S_0$. Arising from the orbital-Zeeman Hamiltonian, $\hat{\boldsymbol{l}}_i = \boldsymbol{r}_{\mathrm{i}} \times \boldsymbol{p}_{\mathrm{i}}$ is the orbital angular momentum of electron i with respect to the global origin (introducing a gauge dependence). As a consequence of the approximated spin–orbit coupling, $\xi(r_{iA})$ is introduced as a spacial operator depending on the internal coordinate $r_{iA} = |\boldsymbol{r}_i - \boldsymbol{R}_A|$ with $\boldsymbol{r}_i$ being the electronic coordinate of electron i and $\boldsymbol{R}_A$ the nuclear coordinate of nucleus A. Hence, $\hat{\boldsymbol{l}}_{iA}$ is the orbital angular momentum operator of electron i with respect to nucleus A and $\hat{\boldsymbol{s}}_i$ the spin angular momentum operator of electron i.[69] It should be noted that the relation only holds for cases where the ground state is energetically well separated from the excited state manifold.[69,73] Even though the form of eqn (4) is suited for decoding the origin of the Δg-shift in terms of the energy level diagrams taking unrestricted molecular orbitals (MOs) into account, the infinite SOS and the inaccessible complete BO eigenspectrum often impede its direct evaluation.[69,73]

In Orca the orbital-Zeeman–spin–orbit coupling contribution to the g-matrix is computed by applying the linear-response theory. From eqn (2) it is clear that the g-matrix can be written as the second derivative of the energy with respect to the magnetic flux density $\boldsymbol{B}$ and the total spin $\boldsymbol{S}$. Treating these quantities as perturbations, a connection can be made between the SOS expression and the spin density matrix $P_{\mu\nu}^{\sigma}$ cast in terms of the MO coefficients with $\sigma = \{\alpha, \beta\}$.[74]

$$\Delta g_{ab}^{(\mathrm{OZ/SOC})} = -\frac{1}{S_0}\sum_{\mu,\nu}\frac{\partial P_{\mu\nu}^{\alpha-\beta}}{\partial B_a}\left\langle\phi_\mu\middle|\hat{h}_b^{\mathrm{SOMF}}\middle|\phi_\nu\right\rangle \quad (5)$$

Rather than using the approximated spin–orbit coupling that emerged in eqn (4), the SOMF theory is applied as indicated by $\hat{h}_{\mathrm{SOMF}}$.[51] The orbitals $\{\phi\}$ represent the atomic orbital (AO) basis set. Connecting the g-factor to the spin density is arguably the most common way to interpret the calculated results in the literature.[75–78] However, while eqn (5) is well suited for a "black box" prediction of the g-matrix, it is less ideal for a detailed analysis due to its rather technical implementation.[74] Thus, eqn (4) constitutes the basis for a semi-quantitative discussion of the origin of the Δg-shift experimentally observed in this study.

3 Results and discussion

3.1 Electric deflection experiments

Fig. 1c–e show the resulting beam profiles of the electric deflection experiments on MSn_{12} (M = Al, Ga, In) at a nozzle temperature of 16 K. A scheme of the experimental setup is shown in Fig. 1a. The experiments with $AlSn_{12}$ and $GaSn_{12}$

were carried out with collimators with a slit width of 400 μm, those with $InSn_{12}$ with a slit width of 200 μm. Isotopically pure tin (^{120}Sn) was used for the experiments on $InSn_{12}$, such that the mass signal of $In^{120}Sn_{12}$ is well separated from the signal of $^{120}Sn_{13}$ in the recorded mass spectra. Note that it was shown for $AlSn_{12}$ that the electric beam deflection is independent of the use of native or isotopically pure tin.[16] To interpret the experimental data, it is important to note that the deflection of the clusters depends on the electronic polarizability and the permanent electric dipole moment, the latter being the structure-sensitive property.[5,35] For rigid clusters, the presence of a permanent dipole moment leads to a broadening of the molecular beam, since the deflecting force depends on the orientation of the dipole moment relative to the electric field. In contrast, the polarizability causes only a single-sided shift of the molecular beam, because the induced dipole moment aligns with the direction of the field.[5,79] In the case of polar clusters (nonvanishing permanent electric dipole moment), which are, additionally, vibrationally excited and therefore the electric dipole moment starts to fluctuate with respect to the body-fixed coordinate system, the broadening of the molecular beam can partially or even completely disappear. This means that the observed mean permanent electric dipole moment is partially or completely quenched due to the floppiness of the clusters.[5,79] Conversely, the detection of a molecular beam broadening always indicates the presence of a polar structural isomer.

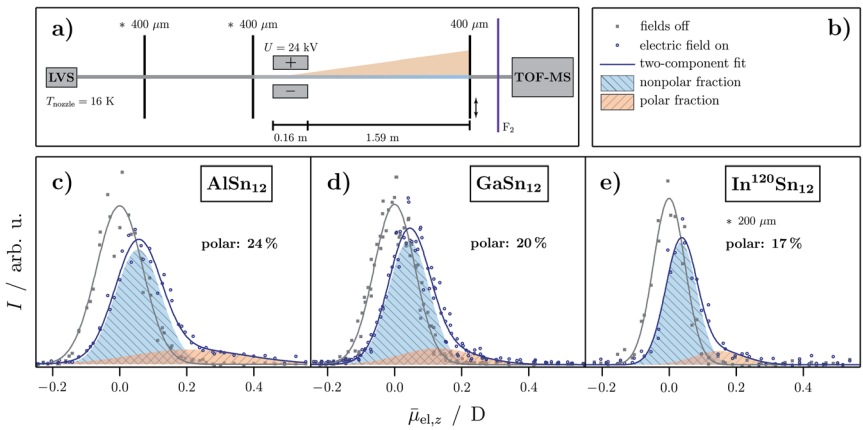

Fig. 1 (a) Scheme of the experimental setup for electric beam deflection experiments with an indicated separation of the molecular beam into a nonpolar (blue) and polar (orange) fraction. Here, the numbers above the collimator slits refer to the slit width. The asterisk indicates that another slit width is used for $InSn_{12}$. (c)–(e) Experimental data of the electric beam deflection given as intensity I as a function of the projection of the observed electric dipole moment on the field direction averaged over the length of the deflection unit and all quantum states $\bar{\mu}_{el,z}$ for MSn_{12} (M = Al,[16] Ga, In) at $T_{nozzle} = 16$ K and a deflection voltage of $U = 24$ kV. The gray squares represent the cluster intensity without applied field whereas blue open circles represent the intensity with applied electric field. Gaussians are fitted to the experimental data (solid lines in the corresponding colors). The nonpolar fraction in the beam profile with applied field is indicated by a shaded blue Gaussian with the same width as the gray one and the polar fraction is shown as a shaded orange area. In (b) the corresponding legend to the graphs is shown.

The beam profiles shown in Fig. 1c–e can be interpreted by the presence of a nonpolar main component, which accounts for 76% to 83% of the total cluster intensity. This component only leads to a shift of the molecular beam. The remaining part comes from a polar fraction, whose beam profile is shifted and broadened and is therefore also responsible for the tailing of the molecular beam. The total deflection can be described quantitatively by approximating the amounts of the polar and nonpolar components using two Gaussian functions. Although this procedure is only valid within the framework of first-order perturbation theory,[5] it was shown that this is an appropriate way to analyze the electric beam profiles.[16] Here, the Gaussian function associated with the polar component is shifted and broadened. This analysis results in a proportion of the polar fraction of 24% for $AlSn_{12}$, which decreases to 17% in the case of $InSn_{12}$. Note that on the one hand these percentages serve only as a lower bound, since some part of the polar cluster's deflection can be quenched due to thermal excitation (rotational and vibrational). This will be further discussed in Sec. 3.3. In addition, the permanent dipole moment of the polar fraction appears to be slightly smaller for $GaSn_{12}$ and $InSn_{12}$ than for $AlSn_{12}$, since the broadening of the polar fraction is less evident. In summary, the electric beam profiles indicate the presence of a nonpolar and a polar structural isomer as shown recently for $AlSn_{12}$.[16]

3.2 Magnetic deflection experiments

Fig. 2c–e show the results of the magnetic deflection experiments of MSn_{12} (M = Al, Ga, In) at a nozzle temperature of 16 K. The molecular beam was collimated to 200 μm before deflection for a better separation of the components. Cluster deflection in an inhomogeneous magnetic field depends on both molecular symmetry and vibrational excitation.[12,63] If clusters are thermally excited, the vibrational modes act like an internal heat bath enabling fast spin transitions. Then only a single-sided deflection of the molecular beam is observed, which is quantitatively described by the high-temperature limit of the Brillouin function.[80] For a total spin quantum number $S = 1/2$, taking typical velocities in the flight direction of about 420 m s^{-1} and reasonable vibrational temperatures of $T_{vib} = 45$ K [17] into account, only a shift of $d_{i,z} = 0.035$ mm ($\bar{\mu}_{mag,z} = 0.035\ \mu_B$) is expected under the present experimental conditions, which is significantly smaller than the collimating slit and, therefore, hardly detectable with this apparatus. If the clusters are rigid and highly symmetrical, the molecular beam can split symmetrically into $2S + 1$ beamlets, *i.e.* superatomic magnetic behavior can be observed and the z-component of the magnetic dipole moment is a constant of motion. The beam profile can then be described by $2S + 1$ Gaussians of the same width as the beam profile without applied field. The positions of their centers are then given by

$$\bar{\mu}_{mag,z} = g M_S \mu_B, \tag{6}$$

with the magnetic spin quantum number $M_S = -S, -S + 1, \ldots, S$ and the (isotropic) g-factor. With decreasing molecular symmetry, the beam splitting is reduced and can vanish even for rigid clusters. This is related to an increased density of rotational states and thus an increased number of avoided crossings in the rotational Zeeman diagram, since the spin state can change at each of these

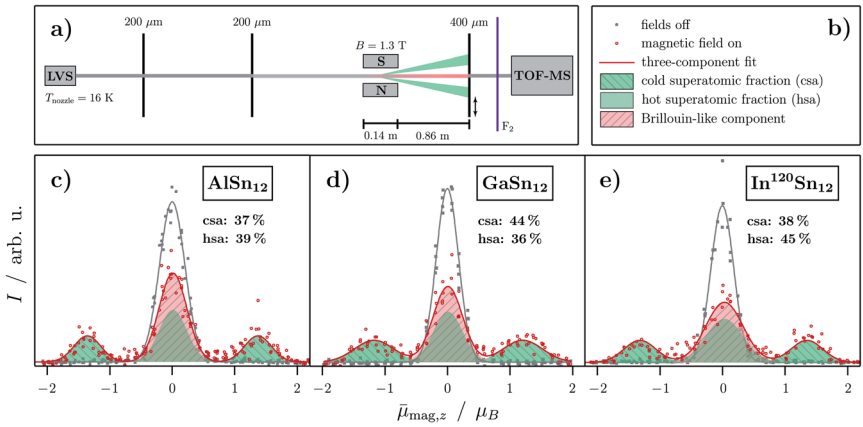

Fig. 2 (a) Scheme of the experimental setup for magnetic beam deflection experiments with an indicated separation of the molecular beam into a Brillouin (red) and superatomic (green) component. (c)–(e) Experimental data of the magnetic beam deflection given as intensity I as a function of the projection of the observed magnetic dipole moment on the field direction averaged over the length of the deflection unit and all quantum states $\bar{\mu}_{\mathrm{mag},z}$ for MSn_{12} (M = Al,[16] Ga, In) at $T_{\mathrm{nozzle}} = 16$ K and an applied magnetic flux density of $B = 1.3$ T. The gray squares represent the cluster intensity without applied field whereas red open circles represent the intensity with applied magnetic field. Gaussians are fitted to the experimental data (solid lines in the corresponding colors). The Brillouin component in the beam profile with applied field is indicated by a shaded red Gaussian and the superatomic components are shown as shaded green areas. The vibrationally-excited nonpolar clusters with quenched superatomic behavior are also depicted in green and referred to as the hot superatomic fraction. In (b) the corresponding legend to the graphs is shown.

avoided crossings while the total angular momentum is conserved. The results in Fig. 2c–e show that the molecular beam splits into three beamlets, with the central part showing almost no deflection and accounting for 56–63% of the total beam intensity. The two outer beamlets at $\bar{\mu}_{\mathrm{mag},z} \approx \pm 1.35\ \mu_B$ account for 37–44%. This fraction of clusters behaves magnetically like an atom with $M_S = \pm 1/2$. Thus, the superatomic clusters represent a spin-1/2 system with values for the g-factor of 2.6–2.7, roughly independent of the doping atom. The strong deviation of the g-factor from the value of the free electron indicates an additional orbital moment in the clusters.[64] In contrast to the splitting of an atomic beam, the beamlets are slightly broadened towards the central peak. This is probably due to rigid clusters changing their spin state within the magnetic field. This occurs because even if the magnetic field is perfectly aligned, the deflection of the clusters covers a range of magnetic flux density of about 30 mT, so that an avoided crossing can be passed through and a spin transition occurs. Because of this, the outer beam components are smeared towards the central peak. This effect seems to be more pronounced for $GaSn_{12}$ and $InSn_{12}$. Whether this is related to the fact that in these experiments the magnet was less optimally aligned than with $AlSn_{12}$ is still unclear. Additionally, it should be mentioned that the magnetic beam deflection of the $AlSn_{12}$ cluster is independent of the use of native or isotopically pure tin.[64]

The central beam component consists of two parts: on the one hand the polar,[16] less symmetrical clusters whose magnetic behavior is described by the

Brillouin function and on the other hand vibrationally-excited nonpolar clusters. This latter fraction is labelled as the hot superatomic fraction in Fig. 2. Here, the vibrational excitation leads to an increased number of avoided crossings such that Brillouin-like behavior also results. It is assumed in each case that the spin state changes at most of the avoided crossings, so that there is only a barely measurable average deflection over the entire flight path in the magnet.[63] The discussion of the *g*-factors in connection with the electronic structure of the clusters in Sec. 3.4 shows that this requirement is very well met in the clusters examined here.

Thus, the hypothesis of two isomers with different polarity allows a coherent explanation of the magnetic deflection results for all cluster species discussed here. As will be shown later, the highly symmetrical structure of the nonpolar isomers consists of a dopant atom (Al, Ga or In) that is endohedrally encapsulated in a Sn_{12} cage (*cf.* Sec. 3.4). Quantum chemical calculations suggest T_h symmetry, *i.e.* the presence of a spherical rotor with low-density (degenerate) rotational states. Hence, the experimentally-observed majority of the nonpolar, vibrationally not excited clusters can fly through the magnet without passing even a single avoided crossing and superatomic behavior is observed. The fractions of vibrationally excited clusters given in Fig. 2 are plausible taking vibrational temperatures around 45 K and wavenumbers for the lowest-lying vibrational modes of 30–50 cm^{-1} into account. With $GaSn_{12}$, for example, one would expect that the amount of vibrationally not excited clusters is about as large as that of the vibrationally excited ones, so that the central beam component in the Stern–Gerlach experiment consists of about 33% polar clusters (regardless of their vibrational state) and about 67% vibrationally excited nonpolar clusters. The magnetic deflection profiles are further discussed in Sec. 3.5 with regard to the avoided-crossing model.

3.3 Double-deflection experiments

To further support the hypothesis that there are two structural isomers present in the molecular beam and to find out how the Stark and Zeeman effects are related for the two isomers, double-deflection experiments were performed.

Fig. 3c and d show how the electric deflection changes for $AlSn_{12}$ when either the superatomic (Fig. 3c) or the Brillouin fraction (Fig. 3d) is filtered out with the help of the Stern–Gerlach magnet. For the investigation of the electric deflection of the Brillouin component, the electric field is permanently applied while the magnetic field is switched on and off. In order to transmit the superatomic fraction, the electric deflector must be shifted slightly as indicated in the scheme of the experiment in Fig. 3b. Additionally, the deflection voltage is increased in both experiments compared to the pure electric deflection experiments, since the field-free path is shorter and a similar deflection can be achieved this way. For the sake of the stability of the cluster intensities the experiments are carried out at $T_{nozzle} = 30$ K, in contrast to $T_{nozzle} = 16$ K in Sec. 3.1 and 3.2. It was shown before that at this nozzle temperature the electric and magnetic deflection is comparable to the experiments at $T_{nozzle} = 16$ K, however, the superatomic fraction is reduced by about 30% for the $AlSn_{12}$ cluster.[16,17] Fig. 3d shows how the beam profile of a superatomic beamlet changes, if the electric field is switched on. Only a displacement of the molecular beam is observed, *i.e.* the tailing has completely

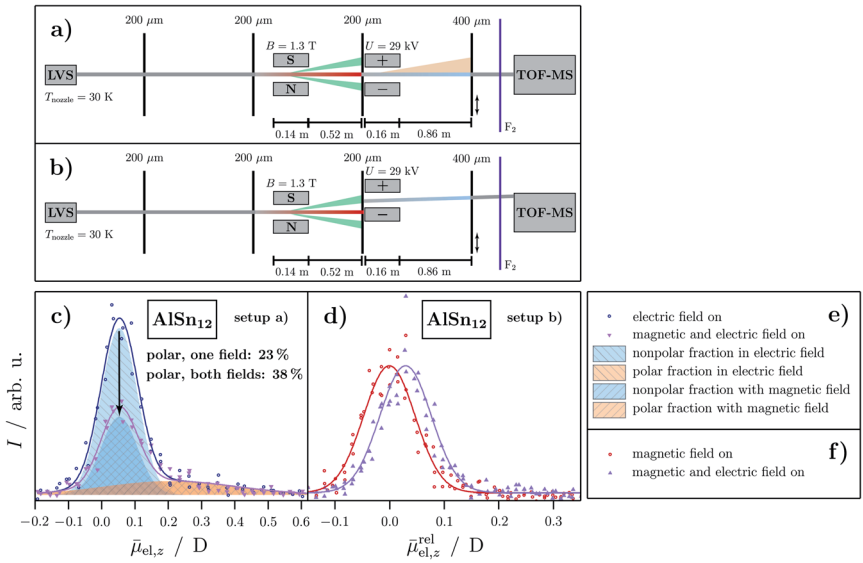

Fig. 3 Schemes of the experimental setup for the combined deflection experiments in which (a) the Brillouin and (b) a superatomic component is further deflected in the electric field. The fractions are indicated in the same color as in the previous figures. Here, too, an additional collimating slit is installed directly in front of the electric deflector to filter out the corresponding fraction. (c) and (d) Experimental data of the combined deflection experiments given as intensity I as a function of the projection of the observed electric dipole moment on the field direction averaged over the length of the deflection unit and all quantum states $\bar{\mu}_{el,z}$ for $AlSn_{12}$ at $T_{nozzle} = 30$ K. Note that the designation of the axis in (d) is changed to a relative projection of the mean electric dipole moment on the direction of the field axis $\bar{\mu}^{rel}_{el,z}$. A magnetic flux density of $B = 1.3$ T and a deflection voltage of $U = 29$ kV are applied. The blue open circles represent the intensity with only the applied electric field whereas the violet upside down triangles show the beam profile with both magnetic and electric field switched on. For the other setup, the red open circles indicate the intensity with only the magnetic field switched on and the violet upright triangles show the intensity with both fields applied. Gaussians are fitted to the experimental data (solid lines in the corresponding colors). The polar and nonpolar fractions are indicated by a shaded blue and orange area, analogous to the color scheme in Fig. 1 while an arrow indicates the reduction of the nonpolar fraction. In (e) and (f) the corresponding legends for the graphs are shown.

disappeared. This observation demonstrates that the superatomic fraction consists exclusively of nonpolar clusters. Since the reference beam profile has been measured with the magnetic field switched on, the designation of the axis is changed to a relative projection of the mean electric dipole moment on the direction of the field axis $\bar{\mu}^{rel}_{el,z}$. In contrast, if the Brillouin fraction is selected by an aperture, then one can clearly see in Fig. 3c that the nonpolar component decreases while the polar component, *i.e.* the tailing, remains constant. However, the nonpolar fraction does not disappear completely which is due to the fact that this component also consists of polar isomers which are thermally excited and, therefore, show a quenched electric dipole moment. From the degree of the decrease of the nonpolar component or the relative increase of the amount of polar clusters, it follows that the number of vibrationally not excited nonpolar clusters is approximately the same as the number of clusters that are vibrationally

excited. Note that the shift and width of the Gaussians for both the polar and nonpolar fraction is the same as in Fig. 1. Therefore, the results of these double-deflection experiments are consistent with the analysis of the Stern–Gerlach experiments in Fig. 2.

Conversely, an enrichment of the nonpolar fraction in the molecular beam by using the electric deflector causes the Brillouin contribution to decrease in the magnetic deflection experiment, as shown in Fig. 4c–e, while the superatomic fraction remains constant. The remaining Brillouin fraction consists of vibrationally excited nonpolar clusters and also of some polar clusters because the electric beam profiles of the two structural isomers partially overlap. It has to be mentioned that the percentage of the superatomic fractions for each cluster species here differs slightly from the ones determined in Sec. 3.2. The deviation is attributed to slight changes in the cluster source settings.[16] However, the trend is the same for all nanoalloy clusters investigated as shown in Fig. 2. The fact that the decrease in the Brillouin component is the smallest for $InSn_{12}$ is due to the fact that the amount of the polar component is lowest for this cluster species. The double-deflection experiments not only support the hypothesis that there are two structural isomers, but also prove that the vibrationally not excited nonpolar clusters behave superatomically, while the polar fraction shows exclusively Brillouin-like behavior.

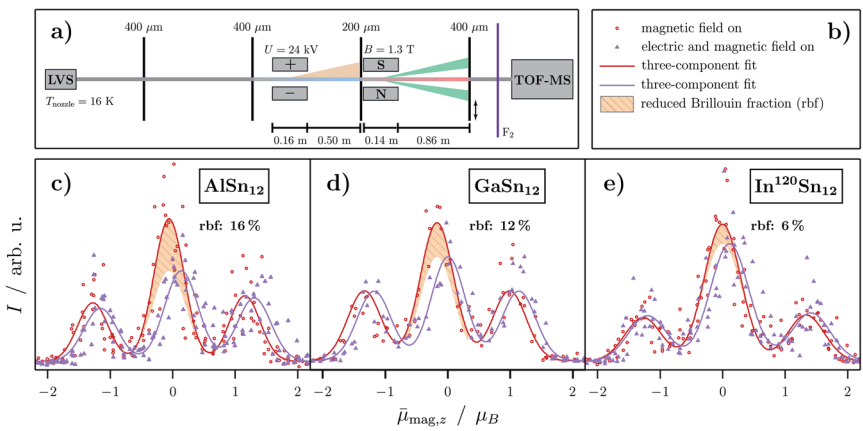

Fig. 4 (a) Scheme of the experimental setup for the combined electric and magnetic beam deflection experiments with the corresponding indicated components in the same color as in the previous figures. Here, an additional collimating slit is installed directly in front of the magnet to increase the separation of the beamlets. (c)–(e) Experimental data of the combined deflection experiments given as intensity I as a function of the projection of the observed magnetic dipole moment on the field direction averaged over the length of the deflection unit and all quantum states $\bar{\mu}_{mag,z}$ for MSn_{12} (M = Al,[16] Ga, In) at T_{nozzle} = 16 K. A deflection voltage of U = 24 kV and a magnetic flux density of B = 1.3 T are applied. The red open circles represent the intensity with only the applied magnetic field whereas the violet upright triangles show the beam profile with both electric and magnetic field on. Gaussians are fitted to the experimental data (solid lines in the corresponding colors). The intensity filtered out by the electric field originating from the polar fraction is indicated by a shaded orange area, analogous to the color scheme in Fig. 1. Note that the overall shift in the beam profile with both fields applied originates from the electric polarizability of the cluster species (*cf.* Fig. 1c–e). In (b) the corresponding legend to the graphs is shown.

3.4 Quantum chemical results

In order to interpret the magnetic behavior quantitatively, a global structure optimization was performed. It turned out that the lowest-lying isomers with $S = 1/2$ are predicted to be those with pyritohedral T_h symmetry (*cf.* Table 1).

In addition, other nonpolar structural isomers with D_{3d} symmetry are also observed, which, however, are higher in energy at the CCSD(T) level of theory. Based on the electric deflection experiments it is not possible to distinguish between these structural isomers, which all have an inversion center and are therefore nonpolar. However, the predicted magnetic properties are sometimes very different. Since the D_{3d} molecular point group corresponds to a symmetrical rotor, the degeneracy of the rotational states is lifted up to a factor of 2 for different values of the magnetic rotational quantum number. Hence, the number of rotational states increases substantially compared to the T_h structure[17] which results in a significantly increased number of avoided crossings in the rotational Zeeman diagram, such that clusters with D_{3d} symmetries are not expected to show superatomic behavior (*cf.* Sec. 3.5). In order to better understand the impact of the symmetry on the electronic structure and the magnetic properties, the transition from an artificial I_h symmetry (not a local minimum) to the T_h symmetry of the GM was systematically investigated taking a "hypothetical" reaction coordinate X into account, *i.e.* $X = +1.00$ at the T_h symmetry of the GM and $X = 0.00$ at the artificial I_h symmetry. This is shown in Fig. 5.

Starting with the GM structure of $AlSn_{12}$ in T_h symmetry ($X = +1.00$), one sees that the singly-occupied α-MO (A_g α-SOMO) consists essentially of 5p-AOs of the Sn atoms. This SOMO is closely related to the triply-degenerate lowest-lying unoccupied MOs (T_g α-LUMO). For the hypothetical case of a singly ionized cluster with I_h symmetry ($X = 0.00$), *i.e.* for I_h-$AlSn_{12}^+$, these four MOs would be degenerate. As can be understood from the SOS expression in eqn (4), the energetic difference $\Delta E = E_{LUMO} - E_{SOMO}$ between the A_g α-SOMO and the triply-degenerate T_g α-LUMO and their similar orbital shapes (due to originating from the same set of orbitals in I_h symmetry) are crucial to the value of the g-factor. The impact of other "transitions", especially those involving the A_g α-LUMO+2 with spin density solely on the Al atom, is found to be insignificant. The energy difference ΔE in particular increases with the magnitude of distortion X with respect to I_h symmetry and with it the g-factor decreases, *i.e.* the g-factor depicts the correlation between geometric and electronic structure. In other words, the dependence of the g-factor on the distortion X can be captured as a consequence of the spin–orbit interaction. The calculated g-factors for the T_h symmetry ($X = +1.00$) agree reasonably well with the experimentally determined value. This also excludes the possibility that the nonpolar clusters in the experiment possess I_h symmetry. However, the calculation of the g-factor for the I_h symmetry should be treated with caution, since the unpaired electron distorts the geometric structure of the degenerate ground state due to Jahn–Teller stabilization and the SOS expression breaks down for nearly degenerate ground states (*cf.* the ESI† for details).

The energy level diagram of $InSn_{12}$ is very similar to that of $AlSn_{12}$. Also for $GaSn_{12}$ the predicted g-factors of the T_h structure agree reasonably well with the experiment. It is interesting, however, that the orbital character of the SOMO changes when the transition to I_h symmetry occurs. For small values of the distortion X, the α-SOMO is now entirely composed of the 4s-AO of the central Ga

Table 1 Overview of the calculated results for the T_h and D_{3d} geometries of MSn_{12} with M = Al, Ga, In. Relative energy differences ΔE are given for the PBE0/def2-TZVPP and CCSD(T)/cc-pVTZ-PP level of theory, while the former is used for the computation of electric dipole moments μ_{el}, isotropic rotational constants $\tilde{B}_{iso}$ and vibrational frequencies $\tilde{\nu}$. The isotropic g_{iso}-factors are calculated at the DKH-PBE0/(SARC-)DKH-def2-TZVPP level of theory and the isotropic hyperfine coupling constants $A_{iso}^{(A)}$ of the central atoms are calculated at the ZORA-PBE0/(SARC-)ZORA-def2-TZVPP level of theory. The isotropic spin–rotation coupling constant Δ_{iso}^{SR} is estimated from the Curl equation (*cf.* eqn(3))

		$AlSn_{12}$		$GaSn_{12}$		$InSn_{12}$	
		T_h	D_{3d}	T_h	D_{3d}	T_h	D_{3d}
		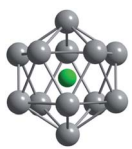		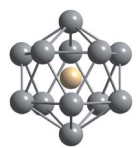		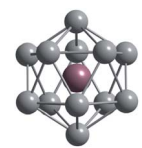	
ΔE^{PBE0}	/eV	0.000	0.007	0.000	0.066	0.004	0.000
$\Delta E^{CCSD(T)}$	/eV	0.000	0.066	0.000	0.190	0.000	0.087
μ_{el}	/D	0.000	0.000	0.000	0.000	0.000	0.000
$\tilde{B}_{iso}$	/m^{-1}	0.194	0.194	0.194	0.193	0.188	0.187
$\tilde{\nu}$	/cm^{-1}	46.79 (t_g)	19.22 (a_{2g})	45.80 (t_g)	27.40 (e_g)	35.01 (t_g)	42.36 (a_{2g})
		58.43 (e_g)	46.82 (e_g)	58.68 (e_g)	31.14 (e_u)	54.24 (e_g)	48.54 (e_u)
		64.58 (e_u)	54.32 (e_u)	65.96 (e_u)	49.25 (a_{2g})	61.09 (t_u)	49.66 (e_g)
		66.67 (t_u)	63.67 (a_{1u})	66.67 (t_u)	58.17 (a_{1g})	71.12 (e_u)	58.28 (a_{1u})
		81.51 (t_g)	72.67 (e_u)	79.55 (t_g)	68.74 (a_{1u})	75.50 (t_g)	69.18 (e_u)
		⋮	⋮	⋮	⋮	⋮	⋮
g_{iso}		2.92	2.90	2.93	2.47	2.92	2.88
$A_{iso}^{(A)}$	/MHz	−5.93 (^{27}Al)	−7.45 (^{27}Al)	0.65 (^{69}Ga)	773.18 (^{69}Ga)	−34.35 (^{115}In)	−27.33 (^{115}In)
Δ_{iso}^{SR}	/10^{-7} eV	−4.46	−4.36	−4.53	−2.26	−4.33	−4.12

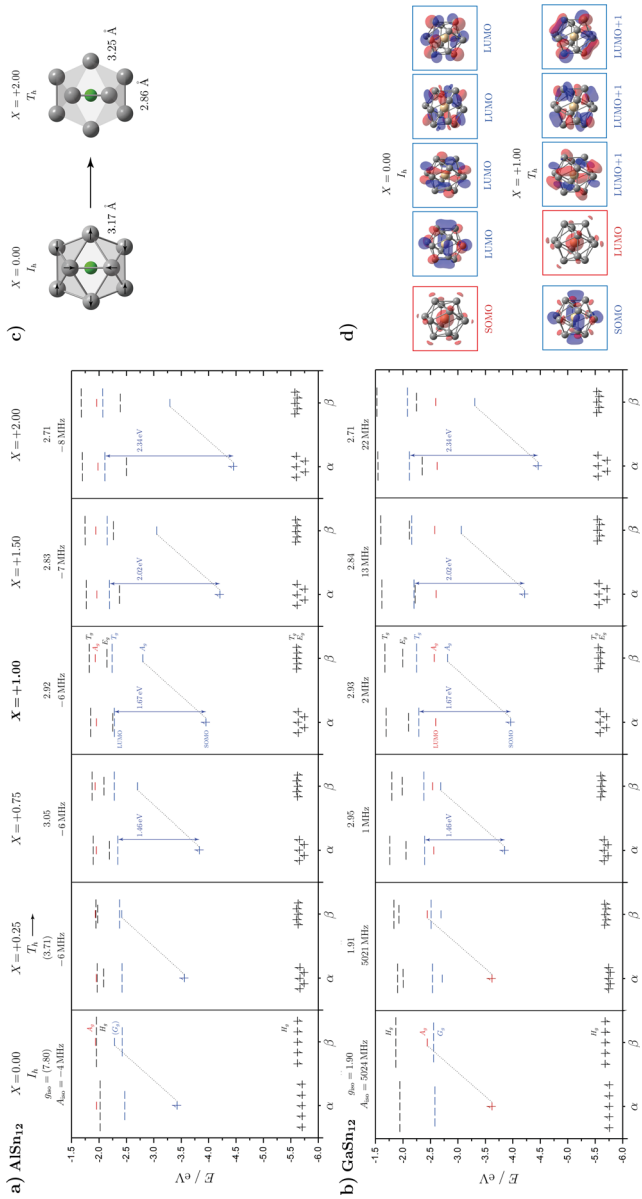

Fig. 5 Spin-unrestricted MO energy diagrams of (a) $AlSn_{12}$ (qualitatively similar to $InSn_{12}$) and (b) $GaSn_{12}$ as a function of the cluster's distortion from I_h towards T_h symmetry. The X-parameter is a measure of the linearly-scaled distortion based on the perfect icosahedron ($X = 0.00$) and the GM structure ($X = +1.00$) as is illustrated for $AlSn_{12}$ in (c). At $X = +2.00$ one set of 6 Sn–Sn bond lengths is compressed by 0.31 Å and another set of the remaining 24 Sn–Sn bonds is elongated by 0.08 Å with respect to the icosahedral Sn–Sn bond length of 3.17 Å. Computed isotropic g_{iso}-factors and hyperfine coupling constants $A_{iso}^{(A)}$ of the central atoms at the DKH-PBE0/(SARC-)DKH-def2-TZVPP and ZORA-PBE0/(SARC-)ZORA-def2-TZVPP level of theory are shown. MOs with spin density solely distributed over the Sn cage are highlighted in blue and those with spin density bounded on the central atom are highlighted in red. Their shape is displayed for $GaSn_{12}$ in (d).

atom. This affects the hyperfine coupling constant $A^{(Ga)}$ of the central atom, which is now increased by 3 orders of magnitude because the Fermi contact term becomes dominant and the spin density is now localized almost exclusively on the Ga atom. In addition, the *g*-factor is now much closer to the value of the free electron, *i.e.* SOC effects have almost completely disappeared. Due to the correlation between geometric and electronic structure, a T_h symmetry can also be clearly assigned to the nonpolar isomer of $GaSn_{12}$.

In conclusion, the large magnitude of the Δg-shift is a consequence of several factors. First, the spin densities of the SOMO and LUMO are very similar, because they stem from the same degenerate set of orbitals in I_h symmetry, and thus the MO coefficients entering eqn (4) (roughly representing the spin densities) are rather large. Second, the LUMO is triply degenerate and adds a factor of three in the SOS expression. Third, the Sn cage contributes with a highly spin–orbit relevant set of atomic orbitals entailing a large SOC constant. Fourth, least significant but still important is the SOMO–LUMO energy difference which is not too large overall.

The SOC which determines the value of the *g*-factor in T_h symmetry of the nonpolar structural isomers is also of great importance for the spin dynamics of the clusters in the Stern–Gerlach magnet. This is because the SOC makes an additional contribution to the spin–rotation coupling. Based on eqn (3), it is possible to take the isotropic value of the *g*-factor into account in order to estimate the contribution to the isotropic spin–rotational coupling constant Δ_{iso}^{SR} that stems from spin–orbit coupling.

$$\Delta_{iso}^{SR} \approx -\frac{\hbar^2 \Delta g_{iso}}{I_{iso}} \tag{7}$$

With the experimentally determined *g*-factor of 2.7 for, *e.g.*, $AlSn_{12}$ and the calculated rotational constant of 0.19 m^{-1}, a value with the magnitude of at least 1×10^{-7} eV results for Δ_{iso}^{SR}. The impact of this value on the spin dynamics of the nanoalloy clusters will be discussed in the next section.

3.5 Avoided-crossing model

To gain a further insight into the magnetic properties of the MSn_{12} (M = Al, Ga, In) clusters, the data given by quantum chemical calculations discussed above can be used to apply a microscopic model based on avoided-crossings in the rotational Zeeman diagram.[60,61] The simulation routine is described elsewhere in detail[62,63] and, therefore, only a brief explanation will be given here. For the nozzle temperatures in the experiments shown in this work, the rotational and spin-Zeeman energies are dominating. For a system with $S = 1/2$, every rotational state splits up in the magnetic field into two different spin-Zeeman levels with $M_S = \pm 1/2$. Due to the manifold of thermally accessible rotational levels, crossings of states with different spin quantum numbers occur. These crossings are avoided if the total angular momentum quantum number in the field direction is conserved.[61,63,81,82] The spin–rotational coupling constant Δ_{iso}^{SR} and the rate of change of the magnetic flux density dB/dt determine if the cluster changes its spin state after passing the crossing. In the case of a diabatic traverse which is favored for small Δ_{iso}^{SR} and high values of dB/dt the spin state

remains unchanged, whereas in the case of an adiabatic traverse the spin state changes. If a change of spin state occurs within the magnetic field, the deflection changes accordingly, *i.e.* superatomic behavior is quenched and only an average deflection is observed. The probability of such a spin-flip is quantitatively given by the Landau–Zener formula in eqn (8).

$$p_{\mathrm{ad}} = 1 - \exp\left(- \frac{\left(\Delta_{\mathrm{iso}}^{\mathrm{SR}}\right)^2}{g_{\mathrm{iso}}\mu_{\mathrm{B}}\hbar\left|M_{\mathrm{S}} - M_{\mathrm{S}'}\right| \dfrac{\mathrm{d}B}{\mathrm{d}t}} \right) \tag{8}$$

With a magnitude of at least 1×10^{-7} eV for $\Delta_{\mathrm{iso}}^{\mathrm{SR}}$ and a rate of approximately $\mathrm{d}B/\mathrm{d}t = 100\ \mathrm{Ts}^{-1}$ a value of $p_{\mathrm{ad}} \approx 100\%$ is obtained. This means that a spin-flip occurs on practically every avoided crossing. However, since the deflection of the clusters is very small within the Stern–Gerlach magnet (~100 μm), the average number of crossings is less than one for clusters with T_{h} symmetry. For the simulation of the magnetic deflection profiles, 5000 particles are generated with randomly chosen magnetic spin quantum numbers M_{S} as well as Boltzmann-weighted rotational angular momentum and vibrational quantum numbers. This is valid since no magnetic field is present in the cluster source. The rotational and vibrational degrees of freedom characterized by the rotational constant $\tilde{B}$ and the vibrational frequencies $\tilde{\nu}$ are then populated using a Boltzmann distribution. This approach might not be exactly true,[83] but is a reasonable assumption for the source used in this work because the clusters are thermalized by the helium carrier gas in the cryogenic nozzle and, therefore, represent a canonical ensemble in the molecular beam deflection experiments.[5,84] However, it was shown that the rotational and vibrational degrees of freedom are cooled with different efficiency[56,59,85] such that two different temperatures must be assumed.

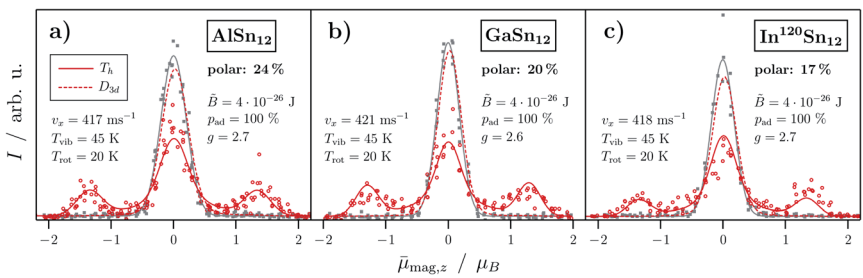

Fig. 6 The simulation of the experimentally measured magnetic deflection based on the avoided-crossing model for both T_{h} (red solid line) and $D_{3\mathrm{d}}$ (red dashed line) symmetry for (a) $AlSn_{12}$, (b) $GaSn_{12}$ and (c) $InSn_{12}$. The intensity I is given as a function of the projection of the observed magnetic dipole moment on the field direction averaged over the length of the deflection unit and all quantum states $\tilde{\mu}_{\mathrm{mag},z}$. The rotational and vibrational temperature T_{rot} and T_{vib} were estimated on the basis of the cluster source parameters whereas the velocity in flight direction v_x is measured directly after the deflection experiments. The values of $\tilde{B}_{\mathrm{iso}}$ and p_{ad} are given by results from quantum chemical calculations (*cf.* Sec. 3.4). The rest of the color code and the symbols are analogous to the ones in Fig. 2.

Fig. 6 shows the resulting simulations based on the avoided-crossing model for the MSn_{12} cluster with M = Al, Ga and In. Here, the simulation is carried out for both isomers with T_h symmetry (nonpolar, spherical rotor) and with D_{3d} symmetry (nonpolar, symmetrical rotor) taking a vibrational temperature of $T_{vib} = 45$ K and a rotational temperature of $T_{vib} = 20$ K into account, which were shown to be reasonable for this cluster source,[17] and considering the quantum chemical parameters presented in Table 1. Additionally, a polar fraction with Brillouin-like behavior was considered. Note that neither the geometrical structure nor the ratio of both isomers in the molecular beam change with applying the magnetic field. The beam profile without applied magnetic field cannot be simulated with respect to the ratio of the isomers, since it is described by a simple Gaussian function independent of the number of isomers present in the molecular beam and their magnetic properties. For the *g*-factors a value of about 2.7 ($AlSn_{12}$ and $InSn_{12}$) and 2.6 ($GaSn_{12}$) is chosen in close agreement with the calculated g_{iso} values. The simulations confirm that the magnetic deflection profiles for all three cluster species show both superatomic and Brillouin-like behavior taking the considered rotational and vibrational temperatures as well as the parameters given by quantum chemical calculations into account. Note that the smearing of the superatomic beamlets towards the central beam component originates from clusters changing their spin state on the path through the magnet and therefore already showing a reduced magnetic moment. Clusters that change their spin state several times within the magnetic field result in the central beamlet and show Brillouin-like behavior. This is already the case for rigid clusters with D_{3d} symmetry as well as for all polar isomers and clusters which are vibrationally excited. These results also demonstrate how crucial the alignment of the Stern–Gerlach magnet is in order to prevent any avoided crossing for at least the majority of the nonpolar clusters.

4 Conclusion and open questions

In this work, electric and magnetic beam deflection experiments were performed on MSn_{12} (M = Al, Ga, In) clusters. Also the magnetic deflection of a molecular beam enriched with nonpolar isomers of MSn_{12} was performed. Additionally, electric beam deflection experiments were carried out separately on the superatomic and Brillouin-like component of the $AlSn_{12}$ cluster for the first time. Not only was the presence of two isomers observed for all cluster species, with one being highly and one less symmetrical, but also the correlation between the superatomic and nonpolar behavior was confirmed. The magnetic properties of these clusters were investigated more thoroughly and a simple semi-quantitative picture could be drawn explaining the abnormally large *g*-factors taking into account the dominant electronic excitation in a SOS treatment. With results obtained by the quantum chemical calculations, the magnetic deflection profiles were simulated on the basis of the avoided-crossing model. The simulations match the experimental results in very good agreement for all cluster species. Here, the quantum chemical calculations give important complementary insight into the magnetic properties of the p-doped tetrel nanoalloy clusters.

A number of polar structural isomers are predicted in the global optimization as well. However, all of these isomers are at least 0.3 eV higher in energy than the global minimum with T_h symmetry. Their presence in the molecular beam experiments is therefore highly improbable (*cf.* the ESI†).[14,86,87] An open question

is therefore what is the geometric structure of the polar fraction? A second question is concerned with the magnitude of the electric dipole moment of the polar isomers and why the corresponding fraction decreases from Al to Ga and In. A methodology that combines deflection experiments with electronic or vibrational spectroscopy might be useful here. With the help of a Stern–Gerlach magnet for example, only the superatomic component could be transmitted *via* an aperture and then examined spectroscopically. The resulting changes in the photodepletion spectra could be directly related to the absorption behavior of the two structural isomers calculated with quantum chemical methods.[38,88] On the one hand, this would then allow an independent confirmation that the nonpolar isomer has T_h symmetry and, on the other hand, the polar isomer could possibly be identified in this way. Hence, by using electric or magnetic deflectors, an isomer-selective spectroscopic investigation of nanoscale bimetal clusters would be conceivable in principle. It is also not yet understood why, for $GaSn_{12}$, the A_g MO solely built from the 4s-AO contribution, as predicted by quantum chemistry, is energetically stabilized to a much larger degree than in $AlSn_{12}$ and $InSn_{12}$. In this context, it would also be interesting to study how the replacement of Sn by Ge and Pb affects the magnetic behavior. Are structures with T_h symmetry also formed that are superatomic? Or is the D_{3d} symmetry preferred so that only a Brillouin-like behavior is observed for these symmetrical rotors? Does the increase in spin–orbit coupling in substituting Sn by Pb result in even larger *g*-factor deviations from the free-electron value? Overall, combined electric/magnetic deflection measurements offer a highly capable tool to uncover correlations in the geometric and electronic structure and thus help to better understand the magnetic behavior of nanoalloy clusters.

Conflicts of interest

There are no conflicts to declare.

Acknowledgements

Financial support for this project was provided by the Deutsche Forschungsgemeinschaft (Grant SCHA 885/16-2). A. L. thanks the Verband der Chemischen Industrie for a scholarship. This work is funded by the Federal Ministry of Education and Research (BMBF) and the state of Hesse as part of the NHR Program.

References

1 W. A. de Heer, *Rev. Mod. Phys.*, 1993, **65**, 611–676.
2 K. D. Bonin and V. V. Kresin, *Electric-Dipole Polarizabilities of Atoms, Molecules, and Clusters*, World Scientific Publishing, Singapore, 1997.
3 J. A. Becker, *Angew. Chem., Int. Ed.*, 1997, **36**, 1390–1404.
4 W. A. de Heer and V. V. Kresin, in *Handbook of Nanophysics: Clusters and Fullerenes*, CRC Press, Boca Raton, 2010, ch. 10.
5 R. Schäfer and S. Heiles, *Dielectric Properties of Isolated Clusters: Beam Deflection Studies*, Springer, Heidelberg, 2014.
6 D. J. Merthe and V. V. Kresin, *J. Phys. Chem. Lett.*, 2016, **7**, 4879–4883.

7 R. Moro, S. Yin, X. Xu and W. A. de Heer, *Phys. Rev. Lett.*, 2004, **93**, 086803.
8 R. Moro, X. Xu, S. Yin and W. A. D. Heer, *Science*, 2007, **1265**, 1265–1270.
9 S. Schäfer, S. Heiles, J. A. Becker and R. Schäfer, *J. Chem. Phys.*, 2008, **129**, 044304.
10 D. A. Götz, A. Shayeghi, R. L. Johnston, P. Schwerdtfeger and R. Schäfer, *Nanoscale*, 2016, **8**, 11153–11160.
11 A. Diaz-Bachs, M. I. Katsnelson and A. Kirilyuk, *New J. Phys.*, 2018, **20**, 043042.
12 U. Rohrmann, P. Schwerdtfeger and R. Schäfer, *Phys. Chem. Chem. Phys.*, 2014, **16**, 23952–23966.
13 Á. Carrera and E. Marceca, *J. Phys. Chem. A*, 2015, **119**, 4207–4213.
14 M. Gleditzsch, L. F. Pašteka, D. A. Götz, A. Shayeghi, R. L. Johnston and R. Schäfer, *Nanoscale*, 2019, **11**, 12878–12888.
15 D. L. Chen, W. Q. Tian, W. C. Lu and C. C. Sun, *J. Chem. Phys.*, 2006, **124**, 154313.
16 F. Rivic, T. M. Fuchs and R. Schäfer, *Phys. Chem. Chem. Phys.*, 2021, **23**, 9971–9979.
17 T. M. Fuchs, F. Rivic and R. Schäfer, *Phys. Rev. A*, 2021, **104**, 012820.
18 S. Schäfer, M. Mehring, R. Schäfer and P. Schwerdtfeger, *Phys. Rev. A: At., Mol., Opt. Phys.*, 2007, **76**, 052515.
19 U. Rohrmann, S. Schäfer and R. Schäfer, *J. Phys. Chem. A*, 2009, **113**, 12115–12121.
20 I. I. Rabi, J. M. B. Kellogg and J. R. Zacharias, *Phys. Rev.*, 1934, **46**, 157–163.
21 J. M. B. Kellogg, I. I. Rabi, N. F. Ramsey and J. R. Zacharias, *Phys. Rev.*, 1939, **56**, 728–743.
22 L. P. Maguire, S. Szilagyi and R. E. Scholten, *Rev. Sci. Instrum.*, 2004, **75**, 3077–3079.
23 M. Jäger, R. Schäfer and R. L. Johnston, *Nanoscale*, 2019, **11**, 9042–9052.
24 P. Giannozzi, S. Baroni, N. Bonini, M. Calandra, R. Car, C. Cavazzoni, D. Ceresoli, G. L. Chiarotti, M. Cococcioni, I. Dabo, A. Dal Corso, S. de Gironcoli, S. Fabris, G. Fratesi, R. Gebauer, U. Gerstmann, C. Gougoussis, A. Kokalj, M. Lazzeri, L. Martin-Samos, N. Marzari, F. Mauri, R. Mazzarello, S. Paolini, A. Pasquarello, L. Paulatto, C. Sbraccia, S. Scandolo, G. Sclauzero, A. P. Seitsonen, A. Smogunov, P. Umari and R. M. Wentzcovitch, *J. Phys.: Condens. Matter*, 2009, **21**, 395502.
25 P. Giannozzi, O. Andreussi, T. Brumme, O. Bunau, M. Buongiorno Nardelli, M. Calandra, R. Car, C. Cavazzoni, D. Ceresoli, M. Cococcioni, N. Colonna, I. Carnimeo, A. Dal Corso, S. de Gironcoli, P. Delugas, R. A. DiStasio, A. Ferretti, A. Floris, G. Fratesi, G. Fugallo, R. Gebauer, U. Gerstmann, F. Giustino, T. Gorni, J. Jia, M. Kawamura, H.-Y. Ko, A. Kokalj, E. Küçükbenli, M. Lazzeri, M. Marsili, N. Marzari, F. Mauri, N. L. Nguyen, H.-V. Nguyen, A. Otero-de-la Roza, L. Paulatto, S. Poncé, D. Rocca, R. Sabatini, B. Santra, M. Schlipf, A. P. Seitsonen, A. Smogunov, I. Timrov, T. Thonhauser, P. Umari, N. Vast, X. Wu and S. Baroni, *J. Phys.: Condens. Matter*, 2017, **29**, 465901.
26 J. P. Perdew, K. Burke and M. Ernzerhof, *Phys. Rev. Lett.*, 1996, **77**, 3865–3868.
27 J. P. Perdew, K. Burke and M. Ernzerhof, *Phys. Rev. Lett.*, 1997, **78**, 1396.
28 J. P. Perdew, M. Ernzerhof and K. Burke, *J. Chem. Phys.*, 1996, **105**, 9982–9985.
29 B. Metz, H. Stoll and M. Dolg, *J. Chem. Phys.*, 2000, **113**, 2563–2569.
30 F. Weigend and R. Ahlrichs, *Phys. Chem. Chem. Phys.*, 2005, **7**, 3297–3305.

31 M. J. Frisch, G. W. Trucks, H. B. Schlegel, G. E. Scuseria, M. A. Robb, J. R. Cheeseman, G. Scalmani, V. Barone, G. A. Petersson, H. Nakatsuji, X. Li, M. Caricato, A. V. Marenich, J. Bloino, B. G. Janesko, R. Gomperts, B. Mennucci, H. P. Hratchian, J. V. Ortiz, A. F. Izmaylov, J. L. Sonnenberg, D. Williams-Young, F. Ding, F. Lipparini, F. Egidi, J. Goings, B. Peng, A. Petrone, T. Henderson, D. Ranasinghe, V. G. Zakrzewski, J. Gao, N. Rega, G. Zheng, W. Liang, M. Hada, M. Ehara, K. Toyota, R. Fukuda, J. Hasegawa, M. Ishida, T. Nakajima, Y. Honda, O. Kitao, H. Nakai, T. Vreven, K. Throssell, J. J. A. Montgomery, J. E. Peralta, F. Ogliaro, M. J. Bearpark, J. J. Heyd, E. N. Brothers, K. N. Kudin, V. N. Staroverov, T. A. Keith, R. Kobayashi, J. Normand, K. Raghavachari, A. P. Rendell, J. C. Burant, S. S. Iyengar, J. Tomasi, M. Cossi, J. M. Millam, M. Klene, C. Adamo, R. Cammi, J. W. Ochterski, R. L. Martin, K. Morokuma, O. Farkas, J. B. Foresman and D. J. Fox, *Gaussian 16, Revision C.01*, 2016.
32 F. Neese, *Wiley Interdiscip. Rev.: Comput. Mol. Sci.*, 2012, **2**, 73–78.
33 F. Neese, *Wiley Interdiscip. Rev.: Comput. Mol. Sci.*, 2018, **8**, 1–6.
34 F. Neese, F. Wennmohs, U. Becker and C. Riplinger, *J. Chem. Phys.*, 2020, **152**, 224108.
35 S. Schäfer, B. Assadollahzadeh, M. Mehring, P. Schwerdtfeger and R. Schäfer, *J. Phys. Chem. A*, 2008, **112**, 12312–12319.
36 B. Assadollahzadeh, S. Schäfer and P. Schwerdtfeger, *J. Comput. Chem.*, 2010, **31**, 929–937.
37 A. Lehr, M. Jäger, M. Gleditzsch, F. Rivic and R. Schäfer, *J. Phys. Chem. Lett.*, 2020, **11**, 7827–7831.
38 A. Lehr, F. Rivic, M. Jäger, M. Gleditzsch and R. Schäfer, *Phys. Chem. Chem. Phys.*, 2022, **24**, 11616–11635.
39 D. A. Götz, A. Shayeghi, R. L. Johnston, P. Schwerdtfeger and R. Schäfer, *J. Chem. Phys.*, 2014, **140**, 164313.
40 S. Heiles, R. L. Johnston and R. Schäfer, *J. Phys. Chem. A*, 2012, **116**, 7756–7764.
41 M. Gleditzsch, T. M. Fuchs and R. Schäfer, *J. Phys. Chem. A*, 2019, **123**, 1434–1444.
42 M. Gleditzsch, M. Jäger, L. F. Pašteka, A. Shayeghi and R. Schäfer, *Phys. Chem. Chem. Phys.*, 2019, **21**, 24478–24488.
43 D. E. Woon and T. H. Dunning, *J. Chem. Phys.*, 1993, **98**, 1358–1371.
44 K. A. Peterson, D. Figgen, E. Goll, H. Stoll and M. Dolg, *J. Chem. Phys.*, 2003, **119**, 11113–11123.
45 C. Riplinger, B. Sandhoefer, A. Hansen and F. Neese, *J. Chem. Phys.*, 2013, **139**, 134101.
46 D. G. Liakos, M. Sparta, M. K. Kesharwani, J. M. Martin and F. Neese, *J. Chem. Theory Comput.*, 2015, **11**, 224108.
47 D. G. Liakos and F. Neese, *J. Chem. Theory Comput.*, 2015, **11**, 4054–4063.
48 C. Riplinger, P. Pinski, U. Becker, E. F. Valeev and F. Neese, *J. Chem. Phys.*, 2016, **144**, 024109.
49 B. Sandhoefer and F. Neese, *J. Chem. Phys.*, 2012, **137**, 094102.
50 F. Neese, *J. Chem. Phys.*, 2001, **115**, 11080–11096.
51 F. Neese, *J. Chem. Phys.*, 2005, **122**, 034107.
52 D. A. Pantazis, X. Y. Chen, C. R. Landis and F. Neese, *J. Chem. Theory Comput.*, 2008, **4**, 908–919.
53 J. D. Rolfes, F. Neese and D. A. Pantazis, *J. Comput. Chem.*, 2020, **41**, 1842–1849.
54 W. de Heer, P. Milani and A. Châtelain, *Z. Phys. D*, 1991, **19**, 241–245.

55 K. Miyajima, S. Yabushita, M. B. Knickelbein and A. Nakajima, *J. Am. Chem. Soc.*, 2007, **129**, 8473–8480.
56 U. Rohrmann and R. Schäfer, *Phys. Rev. Lett.*, 2013, **111**, 133401.
57 U. Rohrmann and R. Schäfer, *J. Phys. Chem. C*, 2015, **119**, 10958–10961.
58 A. Diaz-Bachs, M. I. Katsnelson and A. Kirilyuk, *New J. Phys.*, 2018, **20**, 043042.
59 I. M. Billas, A. Châtelain and W. A. De Heer, *J. Magn. Magn. Mater.*, 1997, **168**, 64–84.
60 X. Xu, S. Yin, R. Moro and W. A. De Heer, *Phys. Rev. Lett.*, 2005, **95**, 237209.
61 X. Xu, S. Yin, R. Moro and W. A. de Heer, *Phys. Rev. B: Condens. Matter Mater. Phys.*, 2008, **78**, 054430.
62 T. M. Fuchs and R. Schäfer, *Phys. Rev. A*, 2018, **98**, 063411.
63 T. M. Fuchs and R. Schäfer, *Phys. Rev. A*, 2019, **100**, 12512.
64 T. M. Fuchs and R. Schäfer, *Phys. Chem. Chem. Phys.*, 2021, **23**, 11334–11344.
65 R. McWeeny, *J. Chem. Phys.*, 1965, **42**, 1717–1725.
66 R. McWeeny and B. Sutcliffe, *Methods of Molecular Quantum Mechanics*, Academic Press, London, 1969.
67 R. McWeeney, *Spins in Chemistry*, Academic Press, New York, 1970.
68 J. E. Harriman, *Theoretical Foundations of Electron Spin Resonance*, Academic Press, New York, 1978.
69 F. Neese and E. I. Solomon, *Inorg. Chem.*, 1998, **37**, 6568–6582.
70 R. F. Curl, *Mol. Phys.*, 1965, **9**, 585–597.
71 G. Tarczay, P. G. Szalay and J. Gauss, *J. Phys. Chem. A*, 2010, **114**, 9246–9252.
72 F. Neese, *J. Chem. Phys.*, 2007, **127**, 164112.
73 F. Neese, in *EPR Spectroscopy: Fundamentals and Methods*, ed. D. Goldfarb and S. Stoll, Wiley, Chichester, 2018, ch. 7.
74 V. A. Tran and F. Neese, *J. Chem. Phys.*, 2020, **153**, 054105.
75 M. Kaupp, C. Remenyi, J. Vaara, O. L. Malkina and V. G. Malkin, *J. Am. Chem. Soc.*, 2002, **124**, 2709–2722.
76 C. Remenyi and M. Kaupp, *J. Am. Chem. Soc.*, 2005, **127**, 11399–11413.
77 M. Witwicki, *ChemPhysChem*, 2015, **16**, 1912–1925.
78 S. Schott, E. R. McNellis, C. B. Nielsen, H. Y. Chen, S. Watanabe, H. Tanaka, I. McCulloch, K. Takimiya, J. Sinova and H. Sirringhaus, *Nat. Commun.*, 2017, **8**, 1–10.
79 R. Moro, R. Rabinovitch, C. Xia and V. V. Kresin, *Phys. Rev. Lett.*, 2006, **97**, 123401.
80 C. Kittel, *Introduction to Solid State Physics*, Wiley, New York, 2005.
81 W. A. De Heer, P. Milani and A. Chtelain, *Phys. Rev. Lett.*, 1990, **65**, 488–491.
82 P. Ballone, P. Milani and W. A. De Heer, *Phys. Rev. B: Condens. Matter Mater. Phys.*, 1991, **44**, 10350–10353.
83 R. E. Smalley, *Laser Chem.*, 1983, **2**, 167–184.
84 X. Xu, PhD thesis, Georgia Institute of Technology, 2007.
85 J. A. Becker and W. A. De Heer, *Ber. Bunsen-Ges. Phys. Chem.*, 1992, **96**, 1237–1243.
86 A. Shayeghi, C. J. Heard, R. L. Johnston and R. Schäfer, *J. Chem. Phys.*, 2014, **140**, 054312.
87 A. Shayeghi, D. A. Götz, R. L. Johnston and R. Schäfer, *Eur. Phys. J. D*, 2015, **69**, 1–5.
88 A. Shayeghi, R. L. Johnston and R. Schäfer, *Phys. Chem. Chem. Phys.*, 2013, **15**, 19715–19723.